Layerwise Stratification and Band Reordering in Twisted Multilayer MoTe₂*

Yueyao Fan*, ¹ Xiao-Wei Zhang*, ¹ Yusen Ye, ¹ Xiaoyu Liu, ¹ Chong Wang, ¹ Kaijie Yang, ¹ Di Xiao, ^{1, 2, †} and Ting Cao^{1, ‡}

¹ Department of Materials Science and Engineering,

University of Washington, Seattle, WA 98195, USA
² Department of Physics, University of Washington, Seattle, WA 98195, USA

We introduce a generalizable, physics-informed strategy for generating training data that enables a machine-learning force field accurate over a broad range of twist angles and stacking layer numbers in moiré systems. Applying this to multilayer twisted MoTe₂ (tMoTe₂), we identify a structural and electronic stratification: the two moiré interface (MI) layers retain substantial lattice reconstruction even in thick multilayers, while outer bulk-like layers show rapidly attenuated distortions. Surprisingly, this stratification becomes strongest not in the ultra-small twist angle regime ($\lesssim 1^{\circ}$), where in-plane domain formation is well known, but rather at intermediate angles (2–5°). Simultaneously, interlayer hybridization across the MI-bulk boundary is strongly suppressed, leading to electronic isolation. In twisted double bilayer MoTe₂, this stratification gives rise to coexisting honeycomb and triangular lattice motifs in the frontier valence bands. We further demonstrate that twist angle and weak gating can create energy shift of bands belonging to the two motifs, producing Chern band reordering and nonlinear electric polarization with modest hole doping. Our approach allows efficient simulation of multilayer moiré systems and reveals structural-electronic separation phenomena absent in bilayer systems.

Moiré superlattices provide a versatile platform for discovering new structural and electronic behaviors in solid state[1]. Their emergent properties, from fractional Chern insulators [2–12] to moiré ferroelectricity [13– 16, are intimately tied to changes in the underlying lattice structure induced by stacking, reconstruction, or symmetry-breaking distortions. Moiré stacking universally induces structural relaxation, which reshapes atomic-scale displacements across a wide range of systems, from graphene [17] to transition-metal dichalcogenide (TMD) homo- and heterostructures[18–20]. In TMD moiré systems, this lattice response is further enriched by strong coupling between mechanical deformations and internal polarization fields, giving rise to emergent topological textures and twist-angle-driven Chernnumber reversal, as supported by both theoretical[21] and experimental studies[2, 22]. Beyond twist angle, the number of stacking layers introduces another powerful degree of freedom to engineer moiré structures: in thick multilayers, layers distant from the moiré interface (MI) can acquire stacking motifs reminiscent of bulk polytypes, such as 2H and 3R in TMD or rhombohedral and Bernal stacking in graphene, creating mixeddimensional architectures that combine moiré-interface and quasi-bulk behaviors, as demonstrated in twisted 1 + n graphene systems[23] and multilayer graphene on BN[6, 24–26].

Despite this progress, how reconstruction and electronic coupling evolve across layers in multilayer moiré superlattices remains incompletely understood, especially in the intermediate twist-angle regime $(2-5^{\circ})$ most

relevant for correlated and topological phases in systems like twisted MoTe₂ (tMoTe₂)[2, 4]. Continuum elasticity suggests that increasing layer thickness would suppress reconstruction since thicker layers are mechanically stiffer, and that any strain or displacement would smoothly decay away from the twisted interface [27–29]. But such descriptions do not capture the distinct stacking energetics between moiré layers, moiré-bulk interfaces, and bulk-like regions, nor the coupled in-plane and out-of-plane strain propagation shaped by both intralayer elasticity and the stacking energetics. A quantitative, atomistic description, serving as a foundation for understanding electronic properties, requires simulations that are both large-scale and stacking-registry aware. Machine-learning force fields (MLFFs) provide the needed scalability and accuracy, yet prior MLFF studies have largely focused on bilayers, where small bilayer supercells or unit cells suffice to provide training data set[21, 30–32]. Multilayer systems such as n + mtMoTe₂ introduce additional R- and H-type interfaces and out-of-plane relaxation that extend beyond adjacent layers, enlarging the configurational space well beyond bilayers and motivating an approach that generalizes across angles and layer numbers.

Here we develop an efficient training data generation strategy for studying n+m tMoTe₂ (Fig. 1(a)) by capturing the complete layer interfaces configurations with 1+2 tMoTe₂ and obtain a MLFF generalizable for twist angles and stacking layers. In multilayer tMoTe₂, we observe structural and electronic layer stratification that are unexpected from continuum elasticity theory. The system stratifies into two motifs, MI layers and bulk-like outer layers. The atomic displacement at MI dominates over that in bulk-like layers at intermediate twist angles, and is robust against increasing layer thickness, indicating layer structural segregation. Electronically, the

^{* *}These two authors contribute equally to this work.

[†] dixiao@uw.edu

[‡] tingcao@uw.edu

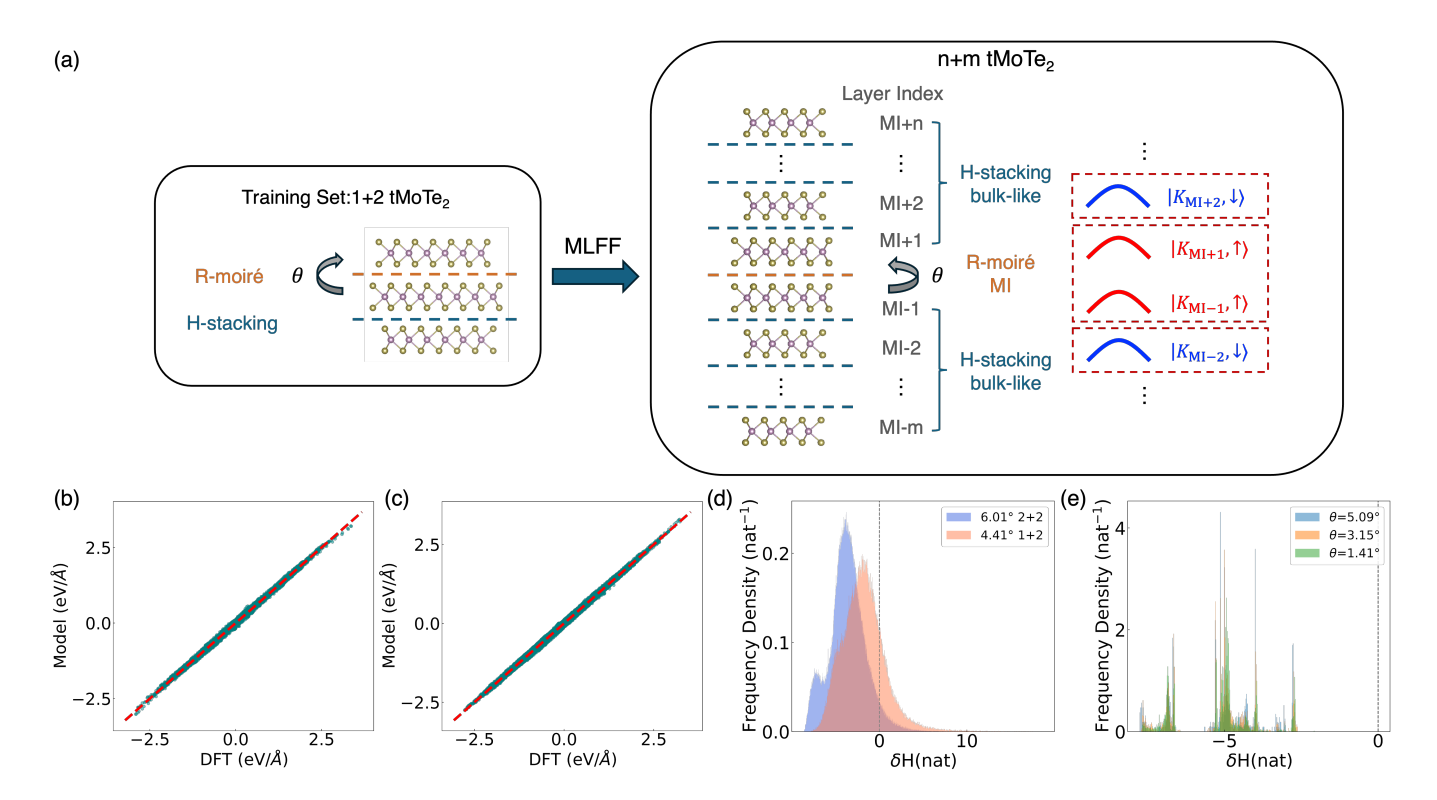


FIG. 1. (a) Schematic structure of n+m tMoTe₂ with twist angle θ near R stacking. Layers are indexed as MI-m to MI+n. Inset: (Right) layer-resolved bands color-coded by layer polarization with red at MI and blue at bulk-like layers. $|K_{\text{MI}+j},\uparrow\rangle\downarrow\rangle$ shows the monolayer state at Brillouin zone corner K of the layer MI+j with spin $\uparrow\downarrow$. (Left) 1+2 tMoTe₂ for training data generation. (b) Force parity plot for MLFF tested on 4.41° 1+2 tMoTe₂, comparing the MLFF-model predicted and DFT calculated ionic forces on each atom (green dots). Red line of y=x shows conditions of exact match. (c) Force parity plot for 6.01° 2+2 tMoTe₂. (d, e) Differential information entropy distribution of local atomic environment for (d) 4.41° 1+2 (red), 6.01° 2+2 (blue), and (e) 5+5 tMoTe₂ under $\theta=5.09^\circ$ (blue), 3.15° (orange), and 1.41° (green) relative to 1+2 training set. Frequency density is the normalized distribution of δH datapoints over the full range.

frontier valence bands are isolated due to negligible interlayer tunneling across MI-bulk boundary. Demonstrated in 2+2 tMoTe₂, the orbitals in MI form a hexagonal pattern and those in outer layers form triangular ones, respectively. The bands from the two motifs show different valley Chern numbers and can flip order in energy by varying twist angles. Furthermore, at modest hole doping, a weak out-of-plane electric field can induce a nonlinear polarization by shifting the holes between the two motifs.

Layerwise transferable MLFF- The lattice reconstruction of n+m multilayer $tMoTe_2$ across twist angles could be predicted by MLFF trained on 1+2 $tMoTe_2$ at a single twist angle which contains a near-complete set of layer interface configurations. The key principle is that MLFF uses local atomic descriptors that encode the embedded local environment of each atom, including both its intralayer coordination and the registry with adjacent layers. As long as all relevant local atomic environments are present in the training set, the model can be reliably transferred to larger and thicker moiré systems.

Fig. 1(a) shows the structure of n + m multilayer tMoTe₂, where n layer-2H stacking MoTe₂ is twisted on the top of m layers of 2H stacking MoTe₂ with an angle

 θ , forming a R-type MI in between. Counting from the layer above MI, the layers are labeled by MI + 1, MI + 2, ..., MI + n and the layers below are denoted as MI – 1 to MI – m.

Assuming the lattice reconstruction in moiré systems is mainly decided by interactions between adjacent layers [33–35], the distinct types of lattice interface configuration in n+m tMoTe₂ are the one R-type MI and multiple 2H interfaces in bulk-like layers. Thus, we could generate the training set of MLFF on one R-type MI and one 2H interface, with the minimal system containing both being 1 + 2 tMoTe₂ (Fig. 1(a)). Compared to training separately on a bilayer moiré R-type and a bilayer 2H system, the 1+2 structure provides advantages: (1) it is balanced between the two types of interfaces and easy to prepare, and (2) it partially incorporates the effect of interactions beyond nearest-neighbor layers, making it more representative for multilayer systems. We then generate training data on 1 + 2 tMoTe₂ at $\theta = 6.01^{\circ}$ by running 5500 steps of ab initio molecular dynamics (AIMD) at 500K and randomly sample 80% of the snapshots for training (see Supplementary Information).

Our trained MLFF can accurately generate lattice reconstruction patterns in n+m tMoTe₂ across various

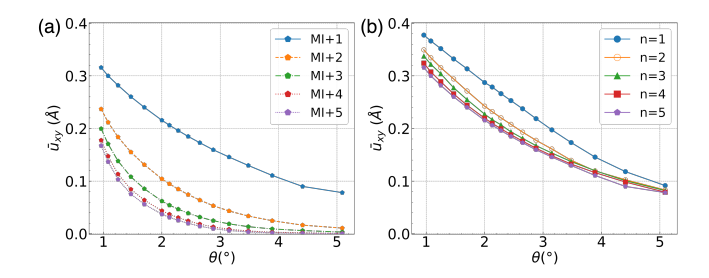


FIG. 2. (a) The average magnitude of the Mo in-plane displacement \bar{u}_{xy} across twist angles and layer indices in 5+5 tMoTe₂. (b) \bar{u}_{xy} at MI layers across twist angles and thickness in n+n (n=1,2,...,5) tMoTe₂. Lines are guides to the eye.

twist angles and layer thickness. To prove MLFF's transferability across twist angles, we test its force predictions on a set of trajectory of 4.41° 1+2 tMoTe₂ against DFT-calculated forces. Fig. 1(b) shows the corresponding parity plot, where the predicted forces align closely with DFT values. The model's strong performance is further quantified by a force root-mean-square error (RMSE) below 0.03 eV/Å. We also validate the MLFF's transferability across layer thicknesses using 6.01° 2+2 tMoTe₂. Parity plot in Fig.1(c) shows agreement between MLFF predictions and DFT results, yielding a force RMSE below 0.04 eV/Å.

The MLFF's transferability roots in the completeness of the training set, which could be quantified by the negative differential information entropy, δH , a measure of how closely the local atomic environments in the target system match those in the training data[36]. Fig.1(d) shows the distribution of δH for local atomic environment in the AIMD calculations of 4.41° 1 + 2 tMoTe₂ and 6.01° 2 + 2 tMoTe₂, with > 80% and > 95% of datapoints exhibiting negative values, respectively (see Supplementary Information).

This high coverage of atomic environment in the training set enables the MLFF to be reliably extended to large, multilayer structures beyond the computational reach of direct DFT relaxation. Fig.1(e) shows the δH distribution of relaxed 5+5 tMoTe₂ structures at $\theta=1.41^\circ, 3.15^\circ$ and 5.09° with > 99% of local environment having negative δH , confirming the training set completeness and indicating reliable MLFF predictions for thick-layer systems.

Structural stratification- The in-plane atomic displacement shows stratification between MI layers and bulk-like layers. Fig.2(a) shows the average magnitude of layerwise Mo in-plane atomic displacement (\bar{u}_{xy}) across θ obtained by MLFF for the layers above MI in 5+5 tMoTe₂, while the layers below MI have the same \bar{u}_{xy} due to an in-plane two-fold rotational symmetry. The in-plane atomic displacement patterns reveal that reconstruction displacement vectors belonging to each layer exhibit characteristic winding patterns around three-fold symmetric axes that switch helicity when crossing MI (see Supplementary Information). Despite the similarity in the displace-

ment pattern, the MI layers, i.e., MI \pm 1, hold the largest \bar{u}_{xy} with a nearly constant drop of 0.1 Å to the bulk-like layers across the twist angle range of 2-5°. The drop is much larger than the attenuation of \bar{u}_{xy} across the bulk-like layers from MI+2 to MI+5, indicating a segregation between the R-type MI and the H-type bulk-like layers. This sharp reconstruction gradient from MI±1 to MI±2 layers contradicts the naïve expectation of gradual strain propagation according to the elasticity of a continuum medium.

Surprisingly, the stratification becomes strongest at intermediate angles (2–5°), rather than at smaller twist angle of $\lesssim 1$ °, where moiré reconstruction becomes significant and in-plane domain formation is observed [15, 18, 20, 37, 38]. For example, at 3.89° 5 + 5 tMoTe₂, \bar{u}_{xy} at the MI+1 layer is 4.5 times of that at the MI+2 layer. In comparison, at 0.96°, this ratio drops to 1.3. These trends are consistent with a picture in which the shorter moiré period and absence of extended domains at 2–5° tend to limit stress transfer from MI±1 to MI±2, whereas at $\lesssim 1$ ° the enlarged moiré cells and domain networks provide longer strain propagation paths, so MI±2 displacements can approach those at MI±1.

The in-plane atomic displacement at MI layers is robust against increasing layer thickness for all twist angles. As shown in Fig. 2(b), when one 2H stacking layer is added at each side to 1+1 tMoTe₂, the \bar{u}_{xy} at MI layers in 2+2 tMoTe₂ keeps > 85% of the \bar{u}_{xy} at 1+1 tMoTe₂. When layer thickness increases from n=2 to 5 in n+n tMoTe₂, the \bar{u}_{xy} curves are almost overlapping, indicating that \bar{u}_{xy} plateaus. As such, the small effect from bulk-like layers to MI±1 layers are dominated by MI±2, while that of the disjoint layers is even smaller. This further validates our training data generation strategy that 1+2 tMoTe₂ composing of both moiré R-type and bilayer 2H-type interfaces provides complete description of atomic environment in thick moiré layers.

Electronic stratification and Chern band reordering- In the following, we focus on the electronic structures of a minimal system that exhibits structural stratification, 2+ 2 tMoTe₂. The frontier orbitals in 2+2 tMoTe₂ is located in either the MI layers (MI ± 1) or outer layers (MI ± 2) with little interlayer tunneling across the 2H interface in between. Fig.3(a) shows the valence bands of $2.88^{\circ} 2 + 2$ tMoTe₂ with layer polarization $S(\alpha, \mathbf{k}) = \sum_{i} |\phi_{i,\alpha,\mathbf{k}}|^2 l_i$. $\phi_{i,\alpha,\mathbf{k}}$ is the projection coefficient of the eigenstate $\psi_{\alpha,\mathbf{k}}$ for band α and momentum **k** onto atomic orbital i (each α represents a set of two-valley degenerate bands, see Supplementary Information). The layer polarization is taken as $l_i = -1$ if i belongs to atoms in MI ± 2 , or $l_i =$ 1, if belonging to MI \pm 1. Our calculations reveal clear electronic stratification, with $S(\alpha, \mathbf{k}) > 0.9$ or < -0.9 for the first four frontier bands, all strongly layer-polarized due to weak interlayer hybridization across the MI-bulk interface (red dashed box in Fig. 1(a)).

This layerwise electronic stratification manifests in coexisting motifs. Fig.3(b) shows the γ point electron density of bands (MI,1) and (MI,2) projected to each layer. Positions of peaks density reveal that electrons distributed at MI ± 1 layers combine together to form a hexagonal electronic lattice pattern. For bands (B, 1) and (B, 2), as shown in Fig.3(c), electrons mostly localize at the outer layers that are spatially separated by MI ± 1 layers. The peak of the electron density at each layer forms a triangular lattice pattern. As such, the negligible interlayer tunneling among MI -2, MI ± 1 , and MI +2 leads to coexistence of two lattice motifs in the frontier valence bands: one honeycomb in (MI, 1) - (MI, 2), and two triangular in (B, 1) and (B, 2).

Decreasing twist angle introduces Chern bands reordering of the states belonging to the two lattice motifs in 2+2 tMoTe₂. When decreasing θ from 2.88° (Fig. 3(a)) to 2.65° (Fig. 3(d)), the energy of band (B, 1) and (B, 2) lifts and almost overlaps with (MI, 1) over the moiré Brillouin zone. Further reducing θ to 2.28° (Fig. 3(e)) brings (B, 1) and (B, 2) to the top valence bands with a global gap over (MI, 1), leading to reordering of bands from the two lattice motifs.

Meanwhile, bands (MI, 1) and (MI, 2) both carry valley Chern number $C_K = 1$ in a wide range of $2 - 3^{\circ}$, while bands (B, 1) and (B, 2) overlap in energy and show combined trivial topology. Thus, the reordering with decreasing twist angle also leads to a change of valley Chern number of the top valence bands. Notably, (MI, 2) forms a flat Chern band with a bandwidth of 3 meV (Fig. 3(d)) at 2.65° , larger than the 2.0° , where the second valence band in 1 + 1 tMoTe₂ attains optimal flatness[21, 39]. This upward shift improves experimental accessibility of the correlated topological phases at higher bands by mitigating twist-angle disorder and enhancing interaction effects via reduced moiré site spacing [9, 39, 40].

Gate-tunable nonlinear electric polarization- The layer polarization at valence band maxima (VBM) is also tunable by out-of-plane electric field E_z causing band reordering. We calculate the band structure of 2+2 tMoTe₂ for a range of twist angles and under E_z , using continuum models fitted to DFT bands (see Supplementary Information). At 2.88° , a very weak field of $E_z = -3.3$ mV/nm (corresponding to an interlayer potential difference of 2.3 meV) drives the bands (B,1) and (MI,1) into near degenerate at κ (Fig. 4(a)). With slightly stronger fields, band (B,1) shifts above (MI,1), switching the VBM layer polarization from the MI layers (Fig. 3(a)) to outer layers (Fig. 4(a)).

The electrically driven band reordering introduces non-linear electric polarization upon light hole doping. At a doping level $\nu = -0.4$, Fig. 4(b) shows the out-of-plane electric polarization per hole, p_z , which exhibits a turning point at $|E_z| \sim 2.0$ mV/nm. Here, $p_z = \sum_{j,\alpha,\mathbf{k}} |\tilde{\psi}_{j,\alpha,\mathbf{k}}|^2 f(\epsilon_{\alpha,\mathbf{k}}) \bar{z}_j/(\nu N)$, where j indexes layer MI + j, $\tilde{\psi}_{j,\alpha,\mathbf{k}}$ is the projection of eigenstates on layer MI+j, $f(\epsilon_{\alpha,\mathbf{k}})$ is the Fermi-Dirac distribution, $\epsilon_{\alpha,\mathbf{k}}$ is the eigen energy, \bar{z}_j is the average z coordinate of layer MI+j, and νN is the number of doped holes. At small $|E_z|$, p_z is dominated by contributions from MI ± 1 , consistent with hole occupation of band (MI, 1). Beyond the

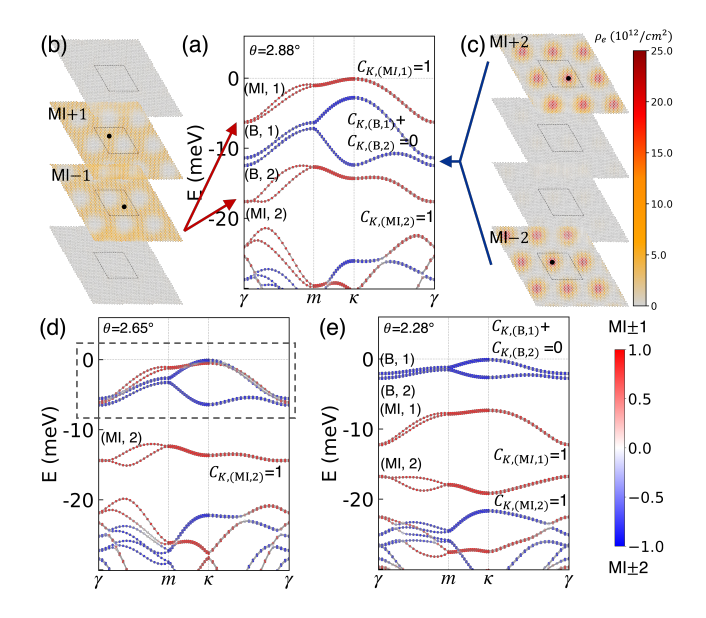


FIG. 3. (a) Band structure of 2.88° 2 + 2 tMoTe₂ with color coded layer polarization $S(\alpha, \mathbf{k})$ (defined in main text). $C_{K,\alpha}$ labels the valley Chern number. (b, c) Electron density ρ_e of states at γ , integrated along z and projected onto 2D. (b) $|\psi_{(\text{MI},1),\gamma}|^2 + |\psi_{(\text{MI},2),\gamma}|^2$ and (c) $|\psi_{(\text{B},1),\gamma}|^2 + |\psi_{(\text{B},2),\gamma}|^2$ for 2.88° 2 + 2 tMoTe₂. The density maxima in each layer are marked by black dots. The moiré cell is marked by black dashed boxes. (d, e) Valence bands of (d) 2.65° and (e) 2.28° 2 + 2 tMoTe₂. Dashed box in (d) marks overlapping bands (MI, 1), (B, 1), and (B, 2).

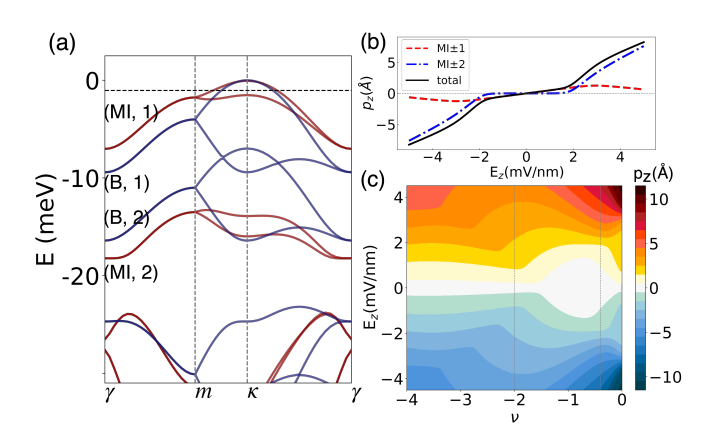


FIG. 4. (a) Valence bands of $2.88^{\circ} 2 + 2$ tMoTe₂ under $E_z = -3.3$ mV/nm. Red and blue bands are layer polarized at MI \pm 1 and MI \pm 2, respectively. A chemical potential corresponding to filling factor $\nu = -0.4$ is marked by black dashed line. (b) The response of out-of-plane electric polarization per hole p_z to out-of-plane electric field E_z at hole filling $\nu = -0.4$. The total value, contributions from MI \pm 1 and MI \pm 2 are marked with black solid, red dashed, and blue dashed lines, respectively. (c) Color map of the total electric polarization per hole p_z as a function of hole filling factors and out-of-plane electric fields.

turning point, p_z follows contributions from MI \pm 2, reflecting hole transfer into (B, 1). The abrupt redistribution of charge between electronically isolated layers produces the nonlinear p_z response. The turning point $|E_z|$ can be further reduced at a slightly smaller twist angle.

Unlike in 1+1 moiré systems where the layer polarization arises from continuous modulation of interlayer wavefunction weights due to field-induced interlayer potential bias, the nonlinear response in 2+2 tMoTe $_2$ is governed by discrete hole transfer between electronically isolated layers, driven by band reordering under electric field. This switch, accompanied by a transition from the honeycomb-like lattice motif to the triangular ones, occurs under an order-of-magnitude smaller fields than in 1+1 tMoTe $_2$ [41], highlighting a strong layer-band selectivity and the sensitive coupling between topology and out-of-plane electric polarization.

The nonlinearity of electric polarization persists in a boarder range of doping level. Fig. 4(c) is a map of p_z over varied doping levels and out-of-plane electric fields, with Fig. 4(b) as the vertical dashed line at $\nu = -0.4$. Besides, at the dashed line $\nu = -2$, we also observed nonlinearity originated from the band reordering between (B, 1) and (B, 2) (see Supplementary Information for details).

Conclusions- We introduce a minimal-layer training protocol that enables a single MLFF to generalize across layer counts and twist angles. This approach uncovers robust layerwise structural and electronic stratification absent in bilayer moiré, leading to Chern band reordering and gate-tunable nonlinear polarization. The coexistence of distinct lattice motifs suggests a broader land-

scape of emergent phases, where Chern bands in the honeycomb MI layers may be further reshaped by charge or magnetic ordering, as well as screening environments in the surrounding triangular lattices upon doping [42–49]. Our finding provides new physical mechanisms to engineer emergent moiré physics in twisted multilayers.

ACKNOWLEDGMENTS

This work is supported by the U.S. Department of Energy, Office of Basic Energy Sciences, under Contract No. DE-SC0025327. The development of machine-learning enabled methods and advanced codes was supported by the Computational Materials Sciences Program funded by the U.S. Department of Energy, Office of Science, Basic Energy Sciences, Materials Sciences, and Engineering Division, PNNL FWP 83557. Y.F was supported by the U.S.-Japan University Partnership for Workforce Advancement and Research and Development in Semiconductors (UPWARDS). This research used resources of the National Energy Research Scientific Computing Center, a DOE Office of Science User Facility supported by the Office of Science of the U.S. Department of Energy under Contract No. DE-AC02-05CH11231 using NERSC award BES-ERCAP0032546 and BES-ERCAP0033256. This work was also facilitated through the use of advanced computational, storage, and networking infrastructure provided by the Hyak supercomputer system and funded by the University of Washington Molecular Engineering Materials Center at the University of Washington (DMR-2308979).

- [1] K. P. Nuckolls and A. Yazdani, A microscopic perspective on moiré materials, Nat. Rev. Mater. 9, 460 (2024).
- [2] J. Cai, E. Anderson, C. Wang, X. Zhang, X. Liu, W. Holtzmann, Y. Zhang, F. Fan, T. Taniguchi, K. Watanabe, Y. Ran, T. Cao, L. Fu, D. Xiao, W. Yao, and X. Xu, Signatures of fractional quantum anomalous hall states in twisted MoTe2, Nature 622, 63 (2023).
- [3] Y. Zeng, Z. Xia, K. Kang, J. Zhu, P. Knüppel, C. Vaswani, K. Watanabe, T. Taniguchi, K. F. Mak, and J. Shan, Thermodynamic evidence of fractional chern insulator in moiré MoTe2, Nature 622, 69 (2023).
- [4] H. Park, J. Cai, E. Anderson, Y. Zhang, J. Zhu, X. Liu, C. Wang, W. Holtzmann, C. Hu, Z. Liu, T. Taniguchi, K. Watanabe, J.-H. Chu, T. Cao, L. Fu, W. Yao, C.-Z. Chang, D. Cobden, D. Xiao, and X. Xu, Observation of fractionally quantized anomalous hall effect, Nature 622, 74 (2023).
- [5] F. Xu, Z. Sun, T. Jia, C. Liu, C. Xu, C. Li, Y. Gu, K. Watanabe, T. Taniguchi, B. Tong, J. Jia, Z. Shi, S. Jiang, Y. Zhang, X. Liu, and T. Li, Observation of integer and fractional quantum anomalous hall effects in twisted bilayer MoTe2, Phys. Rev. X. 13 (2023).
- [6] Z. Lu, T. Han, Y. Yao, A. P. Reddy, J. Yang, J. Seo, K. Watanabe, T. Taniguchi, L. Fu, and L. Ju, Fractional

- quantum anomalous hall effect in multilayer graphene, Nature **626**, 759 (2024).
- [7] Y. Xie, A. T. Pierce, J. M. Park, D. E. Parker, E. Khalaf, P. Ledwith, Y. Cao, S. H. Lee, S. Chen, P. R. Forrester, K. Watanabe, T. Taniguchi, A. Vishwanath, P. Jarillo-Herrero, and A. Yacoby, Fractional chern insulators in magic-angle twisted bilayer graphene, Nature 600, 439 (2021).
- [8] S. H. Aronson, T. Han, Z. Lu, Y. Yao, J. P. Butler, K. Watanabe, T. Taniguchi, L. Ju, and R. C. Ashoori, Displacement field-controlled fractional chern insulators and charge density waves in a graphene/hBN moiré superlattice, Phys. Rev. X. 15 (2025).
- [9] H. Park, J. Cai, E. Anderson, X.-W. Zhang, X. Liu, W. Holtzmann, W. Li, C. Wang, C. Hu, Y. Zhao, T. Taniguchi, K. Watanabe, J. Yang, D. Cobden, J.-H. Chu, N. Regnault, B. A. Bernevig, L. Fu, T. Cao, D. Xiao, and X. Xu, Ferromagnetism and topology of the higher flat band in a fractional chern insulator, Nat. Phys. 21, 549 (2025).
- [10] D. Waters, A. Okounkova, R. Su, B. Zhou, J. Yao, K. Watanabe, T. Taniguchi, X. Xu, Y.-H. Zhang, J. Folk, and M. Yankowitz, Chern insulators at integer and fractional filling in moiré pentalayer graphene, Phys. Rev. X.

- **15** (2025).
- [11] J. Dong, L. Liu, J. Zhu, Z. Pan, Y. Hong, Z. Jia, K. Watanabe, T. Taniguchi, L. Du, D. Shi, et al., Observation of integer and fractional chern insulators in high chern number flatbands, arXiv preprint arXiv:2507.09908 (2025).
- [12] N. Morales-Durán, J. Shi, and A. H. MacDonald, Fractionalized electrons in moiré materials, Nat. Rev. Phys. 6, 349 (2024).
- [13] Z. Zheng, Q. Ma, Z. Bi, S. de La Barrera, M.-H. Liu, N. Mao, Y. Zhang, N. Kiper, K. Watanabe, T. Taniguchi, et al., Unconventional ferroelectricity in moiré heterostructures, Nature 588, 71 (2020).
- [14] K. Yasuda, X. Wang, K. Watanabe, T. Taniguchi, and P. Jarillo-Herrero, Stacking-engineered ferroelectricity in bilayer boron nitride, Science 372, 1458 (2021).
- [15] A. Weston, E. G. Castanon, V. Enaldiev, F. Ferreira, S. Bhattacharjee, S. Xu, H. Corte-León, Z. Wu, N. Clark, A. Summerfield, et al., Interfacial ferroelectricity in marginally twisted 2d semiconductors, Nature nanotechnology 17, 390 (2022).
- [16] J. Ding, H. Xiang, W. Zhou, N. Liu, Q. Chen, X. Fang, K. Wang, L. Wu, K. Watanabe, T. Taniguchi, et al., Engineering band structures of two-dimensional materials with remote moiré ferroelectricity, Nature Communications 15, 9087 (2024).
- [17] H. Yoo, R. Engelke, S. Carr, S. Fang, K. Zhang, P. Cazeaux, S. H. Sung, R. Hovden, A. W. Tsen, T. Taniguchi, et al., Atomic and electronic reconstruction at the van der waals interface in twisted bilayer graphene, Nature materials 18, 448 (2019).
- [18] A. Weston, Y. Zou, V. Enaldiev, A. Summerfield, N. Clark, V. Zólyomi, A. Graham, C. Yelgel, S. Magorrian, M. Zhou, et al., Atomic reconstruction in twisted bilayers of transition metal dichalcogenides, Nature nanotechnology 15, 592 (2020).
- [19] M. R. Rosenberger, H.-J. Chuang, M. Phillips, V. P. Oleshko, K. M. McCreary, S. V. Sivaram, C. S. Hellberg, and B. T. Jonker, Twist angle-dependent atomic reconstruction and moiré patterns in transition metal dichalcogenide heterostructures, ACS nano 14, 4550 (2020).
- [20] M. Van Winkle, I. M. Craig, S. Carr, M. Dandu, K. C. Bustillo, J. Ciston, C. Ophus, T. Taniguchi, K. Watanabe, A. Raja, et al., Rotational and dilational reconstruction in transition metal dichalcogenide moiré bilayers, Nature Communications 14, 2989 (2023).
- [21] X.-W. Zhang, C. Wang, X. Liu, Y. Fan, T. Cao, and D. Xiao, Polarization-driven band topology evolution in twisted MoTe2 and WSe2, Nat. Commun. 15, 4223 (2024).
- [22] B. A. Foutty, C. R. Kometter, T. Devakul, A. P. Reddy, K. Watanabe, T. Taniguchi, L. Fu, and B. E. Feldman, Mapping twist-tuned multiband topology in bilayer wse2, Science 384, 343 (2024).
- [23] D. Waters, E. Thompson, E. Arreguin-Martinez, M. Fujimoto, Y. Ren, K. Watanabe, T. Taniguchi, T. Cao, D. Xiao, and M. Yankowitz, Mixed-dimensional moiré systems of twisted graphitic thin films, Nature 620, 750 (2023).
- [24] C. Mullan, S. Slizovskiy, J. Yin, Z. Wang, Q. Yang, S. Xu, Y. Yang, B. A. Piot, S. Hu, T. Taniguchi, et al., Mixing of moiré-surface and bulk states in graphite, Nature 620, 756 (2023)
- [25] Z. Lu, T. Han, Y. Yao, Z. Hadjri, J. Yang, J. Seo, L. Shi,

- S. Ye, K. Watanabe, T. Taniguchi, et al., Extended quantum anomalous hall states in graphene/hbn moiré superlattices, Nature 637, 1090 (2025).
- [26] J. Xie, Z. Huo, X. Lu, Z. Feng, Z. Zhang, W. Wang, Q. Yang, K. Watanabe, T. Taniguchi, K. Liu, et al., Tunable fractional chern insulators in rhombohedral graphene superlattices, Nature Materials, 1 (2025).
- [27] D. Halbertal, L. Klebl, V. Hsieh, J. Cook, S. Carr, G. Bian, C. R. Dean, D. M. Kennes, and D. N. Basov, Multilayered atomic relaxation in van der waals heterostructures, Physical Review X 13, 011026 (2023).
- [28] P. Cazeaux, M. Luskin, and D. Massatt, Energy minimization of two dimensional incommensurate heterostructures, Archive for Rational Mechanics and Analvsis 235, 1289 (2020).
- [29] D. Halbertal, N. R. Finney, S. S. Sunku, A. Kerelsky, C. Rubio-Verdú, S. Shabani, L. Xian, S. Carr, S. Chen, C. Zhang, et al., Moiré metrology of energy landscapes in van der waals heterostructures, Nature communications 12, 242 (2021).
- [30] J. Liu, Z. Fang, H. Weng, and Q. Wu, DPmoire: a tool for constructing accurate machine learning force fields in moiré systems, Npj Comput. Mater. 11 (2025).
- [31] Y. Shaidu, M. H. Naik, S. G. Louie, and J. B. Neaton, Transferable dispersion-aware machine learning interatomic potentials for multilayer transition metal dichalcogenide heterostructures, Npj Comput. Mater. 11 (2025).
- [32] J. D. Georgaras, A. Ramdas, C. H. Shan, E. Halsted, T. Li, F. H. da Jornada, et al., Accurate, transferable, and verifiable machine-learned interatomic potentials for layered materials, arXiv preprint arXiv:2503.15432 (2025).
- [33] H. Wang, L. Zhang, J. Han, and W. E, DeePMD-kit: A deep learning package for many-body potential energy representation and molecular dynamics, Comput. Phys. Commun. 228, 178 (2018).
- [34] J. Zeng, D. Zhang, D. Lu, P. Mo, Z. Li, Y. Chen, M. Rynik, L. Huang, Z. Li, S. Shi, Y. Wang, H. Ye, P. Tuo, J. Yang, Y. Ding, Y. Li, D. Tisi, Q. Zeng, H. Bao, Y. Xia, J. Huang, K. Muraoka, Y. Wang, J. Chang, F. Yuan, S. L. Bore, C. Cai, Y. Lin, B. Wang, J. Xu, J.-X. Zhu, C. Luo, Y. Zhang, R. E. A. Goodall, W. Liang, A. K. Singh, S. Yao, J. Zhang, R. Wentzcovitch, J. Han, J. Liu, W. Jia, D. M. York, W. E, R. Car, L. Zhang, and H. Wang, DeePMD-kit v2: A software package for deep potential models, J. Chem. Phys. 159 (2023).
- [35] S. Batzner, A. Musaelian, L. Sun, M. Geiger, J. P. Mailoa, M. Kornbluth, N. Molinari, T. E. Smidt, and B. Kozinsky, E(3)-equivariant graph neural networks for data-efficient and accurate interatomic potentials, Nat. Commun. 13, 2453 (2022).
- [36] D. Schwalbe-Koda, S. Hamel, B. Sadigh, F. Zhou, and V. Lordi, Model-free estimation of completeness, uncertainties, and outliers in atomistic machine learning using information theory, Nature Communications 16, 4014.
- [37] J. Quan, L. Linhart, M.-L. Lin, D. Lee, J. Zhu, C.-Y. Wang, W.-T. Hsu, J. Choi, J. Embley, C. Young, et al., Phonon renormalization in reconstructed mos2 moiré superlattices, Nature materials 20, 1100 (2021).
- [38] N. Tilak, G. Li, T. Taniguchi, K. Watanabe, and E. Y. Andrei, Moiré potential, lattice relaxation, and layer polarization in marginally twisted mos2 bilayers, Nano Letters 23, 73 (2022).

- [39] C. Wang, X.-W. Zhang, X. Liu, J. Wang, T. Cao, and D. Xiao, Higher landau-level analogs and signatures of non-abelian states in twisted bilayer MoTe_{2}, Phys. Rev. Lett. 134, 076503 (2025).
- [40] K. Kang, Y. Qiu, K. Watanabe, T. Taniguchi, J. Shan, and K. F. Mak, Double quantum spin hall phase in moiré wse2, Nano Letters 24, 14901 (2024).
- [41] E. Anderson, F.-R. Fan, J. Cai, W. Holtzmann, T. Taniguchi, K. Watanabe, D. Xiao, W. Yao, and X. Xu, Programming correlated magnetic states with gate-controlled moiré geometry, Science 381, 325 (2023).
- [42] T. Li, S. Jiang, B. Shen, Y. Zhang, L. Li, Z. Tao, T. Devakul, K. Watanabe, T. Taniguchi, L. Fu, J. Shan, and K. F. Mak, Quantum anomalous hall effect from intertwined moiré bands, Nature 600, 641 (2021).
- [43] Y. Xu, S. Liu, D. A. Rhodes, K. Watanabe, T. Taniguchi, J. Hone, V. Elser, K. F. Mak, and J. Shan, Correlated insulating states at fractional fillings of moiré superlattices, Nature 587, 214 (2020).
- [44] E. C. Regan, D. Wang, C. Jin, M. I. Bakti Utama, B. Gao, X. Wei, S. Zhao, W. Zhao, Z. Zhang, K. Yumigeta, M. Blei, J. D. Carlström, K. Watanabe, T. Taniguchi, S. Tongay, M. Crommie, A. Zettl, and F. Wang, Mott and generalized wigner crystal states in WSe₂/WS₂ moiré superlattices, Nature 579, 359 (2020).

- [45] Y. Tang, L. Li, T. Li, Y. Xu, S. Liu, K. Barmak, K. Watanabe, T. Taniguchi, A. H. MacDonald, J. Shan, and K. F. Mak, Simulation of hubbard model physics in WSe₂/WS₂ moiré superlattices, Nature 579, 353 (2020).
- [46] L. Wang, E.-M. Shih, A. Ghiotto, L. Xian, D. A. Rhodes, C. Tan, M. Claassen, D. M. Kennes, Y. Bai, B. Kim, K. Watanabe, T. Taniguchi, X. Zhu, J. Hone, A. Rubio, A. N. Pasupathy, and C. R. Dean, Correlated electronic phases in twisted bilayer transition metal dichalcogenides, Nature Materials 19, 861 (2020).
- [47] A. Ghiotto, E.-M. Shih, G. S. S. G. Pereira, D. A. Rhodes, B. Kim, J. Zang, A. J. Millis, K. Watanabe, T. Taniguchi, J. C. Hone, L. Wang, C. R. Dean, and A. N. Pasupathy, Quantum criticality in twisted transition metal dichalcogenides, Nature 597, 345 (2021).
- [48] Y. Zhou, J. Sung, E. Brutschea, I. Esterlis, Y. Wang, G. Scuri, R. J. Gelly, H. Heo, T. Taniguchi, K. Watanabe, G. Zaránd, M. D. Lukin, P. Kim, E. Demler, and H. Park, Bilayer wigner crystals in a transition metal dichalcogenide heterostructure, Nature 595, 48 (2021).
- [49] H. Li, S. Li, E. C. Regan, D. Wang, W. Zhao, S. Kahn, K. Yumigeta, M. Blei, T. Taniguchi, K. Watanabe, S. Tongay, A. Zettl, M. F. Crommie, and F. Wang, Imaging two-dimensional generalized wigner crystals, Nature 597, 650 (2021).